


# Dissolution kinetics and rate-controlling mechanism of sintered uranium nitride pellets in nitric acid

Downloaded from: https://research.chalmers.se, 2026-11-07 16:54 UTC

Citation for the original published paper (version of record):
Saad, M., Vollmer, T., Zagoraios, G. et al (2026). Dissolution kinetics and rate-controlling mechanism of sintered uranium nitride pellets in
nitric acid. Journal of Radioanalytical and Nuclear Chemistry, 335(10): 6745-6760.
http://dx.doi.org/10.1007/s10967-026-11182-7

N.B. When citing this work, cite the original published paper.

research.chalmers.se offers the possibility of retrieving research publications produced at Chalmers University of Technology. It covers all kind of research output: articles, dissertations, conference papers, reports etc. since 2004. research.chalmers.se is administrated and maintained by Chalmers Library

(article starts on next page)

Journal of Radioanalytical and Nuclear Chemistry
https://doi.org/10.1007/s10967-026-11182-7

# Dissolution kinetics and rate-controlling mechanism of sintered uranium nitride pellets in nitric acid

**M. Ghaly[1] · Teodora Retegan Vollmer[1] · G. Zagoraios[1] · Esraa Darwish[1] · Christos Andrikopoulos[1] · Marcus Hedberg[1]**

Received: 14 July 2026 / Accepted: 12 September 2026
© The Author(s) 2026

**Abstract**
Uranium nitride (UN) is a promising advanced nuclear fuel material because of its high thermal conductivity and high melting point. Efficient reprocessing of UN is essential for minimizing uranium consumption and reducing the volume and radiotoxicity of nuclear waste. Dissolution is a key step in the reprocessing process. This work investigates the dissolution kinetics of sintered UN pellets in nitric acid. UN powder was synthesized from $UO_2$ powder by carbothermic nitridation and characterized by X-ray diffraction (XRD). Pellets with densities of 90–92.5% of the theoretical density were produced by spark plasma sintering (SPS) at 1923 K and 75 MPa. Dissolution experiments were conducted in 4, 6, and 8 M nitric acid at 323, 343, and 363 K. A dissolution extent of 100% was achieved under several of the investigated conditions. Increasing the nitric acid concentration from 4 to 8 M and the temperature from 323 to 363 K resulted in an increased dissolution rate. Kinetic analysis using the shrinking-core model showed that surface chemical reaction control described the dissolution behavior better than diffusional transport. The apparent activation energies obtained from Arrhenius plots ranged from 22.9 to 35.3 kJ/mol, further indicating that the dissolution process is predominantly controlled by a surface chemical reaction.

**Keywords** Uranium nitride · Dissolution · Kinetics · Shrinking-core shell model

## Introduction

Advanced nuclear fuels are being developed to enhance fuel performance under demanding reactor operating conditions. These conditions include high temperatures and accident scenarios. Among the candidate fuel materials, uranium mononitride (UN) has attracted considerable interest. This is due to its high uranium density and high thermal conductivity. UN also has potential for use in advanced Generation IV reactor systems [1–3].

Closing the nuclear fuel cycle through the recovery and recycling of nuclear materials offers several potential advantages. In the case of irradiated spent nuclear fuel (SNF), reprocessing can recover valuable fissile and fertile materials. This can reduce the demand for uranium mining, conversion, and enrichment at the front end of the fuel cycle [4]. Reprocessing may also decrease the quantity of material requiring disposal as high-level radioactive waste. It can also enable the separation and conditioning of waste constituents into suitable, stable waste forms [5]. Material recovery is also relevant during nuclear-fuel fabrication. Unirradiated fuel pellets may be mechanically defective [6] or fail to meet dimensional, microstructural, or chemical-purity specifications. Whenever feasible, such pellets should be recycled rather than discarded. Efficient recycling of off-specification material can improve resource utilization. It can also minimize the generation of radioactive waste during fuel fabrication.

Rejected fuel pellets can generally be recycled through either dry or wet processing routes. Dry recycling relies primarily on mechanical, physical, and thermal treatments to recover fuel material from off-specification pellets [7, 8]. Such approaches can convert rejected pellets into powders or feedstocks suitable for subsequent fuel refabrication. They are therefore effective when rejection results from dimensional, geometrical, or certain microstructural defects. However, dry recycling generally provides limited capability for removing chemical impurities. In contrast, wet-chemical processing enables both material recovery and chemical purification. This

✉ M. Ghaly
mariamg@chalmers.se

[1] Division of Nuclear Chemistry and Industrial Materials Recycling, Department of Chemistry and Chemical Engineering, Chalmers University of Technology, 412 96 Gothenburg, Sweden

Published online: 28 September 2026

can be achieved, for example, through solvent-extraction-based separation processes [9]. Such processes require efficient dissolution of the fuel matrix in an appropriate aqueous medium. This dissolution must occur before subsequent purification and separation steps.

The dissolution behavior of sintered uranium- and plutonium-oxide fuels has been extensively investigated [10–12]. However, fewer studies have addressed the dissolution chemistry of uranium mononitride [13]. The dissolution of UN is inherently more complex than that of $UO_2$. This is because both the uranium and nitrogen components participate in the reaction chemistry. During dissolution of $UO_2$ in nitric acid, uranium is oxidized from U(IV) to soluble U(VI) species. In contrast, dissolution of UN also involves cleavage and transformation of the uranium–nitrogen framework. This results in the formation of nitrogen-containing aqueous species. Depending on the dissolution conditions, nitrogen originating from UN may be converted into species such as nitrite ($NO_2^-$), nitrate ($NO_3^-$), and ammonium ($NH_4^+$) [1, 14]. Reactive nitrogen intermediates, including nitrous acid ($HNO_2$), may subsequently participate in redox reactions within the dissolution medium. These reactions may influence the overall dissolution kinetics and reaction mechanism.

A detailed understanding of the dissolution behavior of UN is therefore essential. Its dependence on process conditions must also be understood. This knowledge is important for the development of efficient wet-chemical recycling and reprocessing strategies for nitride fuels. In the present study, the dissolution of uranium mononitride in nitric acid was systematically investigated as a function of nitric acid concentration and temperature. The objective was to elucidate the influence of these parameters on the dissolution process.

## The effect of nitric acid concentration and temperature

Previous studies have shown that the dissolution rate of uranium dioxide ($UO_2$) increases with both nitric acid concentration [15–19] and temperature [16, 17]. The dissolution rate typically increases exponentially with temperature, indicating that the rate-determining step involves overcoming an activation-energy barrier. This temperature dependence is commonly described by the Arrhenius equation (Eq. 1).

$$K = Ae^{-E_a/(RT)} \tag{1}$$

Equation 1 can also be expressed in the linearized form shown in Eq. 2, where $k$ is the rate constant, $T$ is the absolute temperature in kelvin, $R$ is the gas constant (8.314 J mol$^{-1}$ K$^{-1}$), and $A$ is the pre-exponential factor.

$$\ln K = \ln A - \frac{E_a}{R} \times \frac{1}{T} \tag{2}$$

## Modeling of the kinetic data

Several models have been developed to describe liquid–solid reaction systems. One of the most widely used approaches for dissolution processes is the shrinking-core model (SCM). In this model, a spherical or cylindrical solid reacts with the surrounding liquid at its surface, and the unreacted core gradually decreases in size as the reaction proceeds. Such behavior is common in leaching, acid dissolution, and hydrometallurgical extraction, where a solid reactant interacts with a liquid reagent to form soluble or removable products [20].

The shrinking-core model is based on the following assumptions:

- The reaction begins at the external surface of the solid and progresses inward with time.
- The particles are assumed to be cylindrical or spherical and to shrink uniformly while retaining their basic geometry.
- The particle core is initially unreacted, while a reacted region develops around it.
- The solid is ultimately consumed, with no residual ash assumed to remain.
- The reaction occurs at the interface between the unreacted solid and the surrounding liquid.
- The system is assumed to remain isothermal.
- The liquid phase is well mixed, so the bulk reactant concentration remains approximately constant.
- Only radial shrinkage is considered; axial changes are assumed to be negligible.

This model captures the principal features of solid dissolution, as illustrated schematically in Fig. 1.

Several rate-controlling mechanisms can be considered. These include transport of the reactant from the bulk liquid to the external surface of the solid, represented by film diffusion (Eq. 3), and diffusion through a reacted product layer (Eqs. 4, 5). The overall rate may also be controlled by the chemical reaction at the interface between the liquid reactant and the unreacted solid (Eqs. 6, 7) [21, 22]. In the following equations, $x$ denotes the fraction dissolved at time $t$, whereas $k_f$, $k_d$, and $k_r$ denote the rate constants associated with film diffusion, product-layer diffusion, and surface reaction control, respectively. Lowercase $k$ is used for these mechanism-specific rate constants to distinguish them from the uppercase $K$ used as the apparent rate constant in the Arrhenius analysis (Eqs. 1, 2).

Film diffusion controls

Spherical or cylindrical geometry $\quad X = k_f t$ (3)

Ash diffusion controls

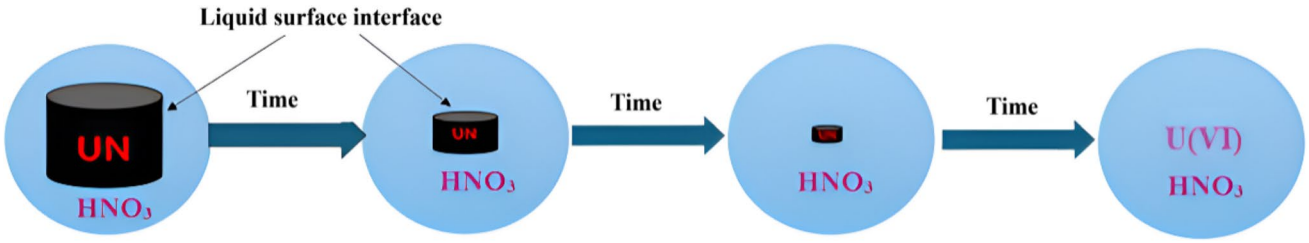



**Fig. 1** Diagram illustrating the dissolution process of UN pellets via SCM

$$\text{Cylindrical geometry} \qquad X + (1-x)\ln(1-x) = k_d t \quad (4)$$

$$\text{Spherical geometry} \qquad 1 + 2(1-x) - 3(1-x)^{2/3} = k_d t \quad (5)$$

Reaction controls

$$\text{Cylindrical geometry} \qquad 1 - (1-x)^{1/2} = k_r t \quad (6)$$

$$\text{Spherical geometry} \qquad 1 - (1-x)^{1/3} = k_r t \quad (7)$$

## Materials and methods

### Fabrication and analysis of UN powder

UN powder was prepared from $UO_2$ powder by carbothermic nitridation. The $UO_2$ powder was mixed with carbon nanopowder (Supelco, approximately 200 nm particle size) in a planetary ball mill (Retsch PM 100) for 1 h at 250 rpm using stainless-steel milling balls. The carbon-to-$UO_2$ molar ratio was 2.3:1. The powder mixture was placed in alumina boats inside an alumina tube furnace (Entech ETF 30–50/18-S). Carbothermic nitridation was performed under flowing $N_2$ containing 5% $H_2$ at 1.6 $dm^3$/min. The sample was heated at 15 K/min to 1823 K and held for 3 h, then heated at 10 K/min to 1873 K and held for 2 h. It was subsequently heated at 10 K/min to 1923 K and held for 1 h. The sample was then cooled at 10 K/min to 1673 K, after which the atmosphere was changed to Ar containing 5% $H_2$ at a flow rate of 1.4 $dm^3$/min. The system was flushed with the Ar–$H_2$ mixture for 0.5 h before further cooling to limit desquamative formation in the material. A cooling rate of 10 K/min was maintained to approximately 873 K. Below this temperature, the sample cooled naturally to room temperature because the furnace was not equipped with an active cooling system.

After cooling, the crucible containing the synthesized UN powder was removed from the tube furnace and transferred to a glove box for storage under an atmosphere containing <0.1 ppm $O_2$ and <0.1 ppm moisture. Transfer from the furnace to the glove-box antechamber was performed in an uncontrolled atmosphere; consequently, the sample was exposed to air for approximately 20–30 s.

Powder X-ray diffraction was used to characterize the synthesized UN powder using a BRUKER D2 PHASER instrument in Bragg–Brentano $\theta$–$2\theta$ geometry with Cu Kα radiation (0.154184 nm) and a LynxEye detector. The X-ray tube was operated at 30 kV and 10 mA, and diffractograms were collected over a $2\theta$ range of 20–144°.

The total carbon content of the UN powder was measured using a LECO CS-744 carbon/sulfur analyzer. Measurements were performed in triplicate. Before analysis, the instrument was calibrated using daily blank and drift calibrations with the LECO steel-pin calibration standard 501–679, containing 0.799 wt% carbon and 0.013 wt% sulfur.

The oxygen content was measured using a LECO TC-436DR analyzer. Triplicate measurements were performed on portions of a polished and crushed UN pellet. The instrument was calibrated using the Degerfors Laboratory Ltd. certified reference material DFS3, containing 3.04 wt% oxygen. Standard leakage testing and blank calibration were also performed before measurement.

### Pellet sintering

UN pellets were sintered using a spark plasma sintering (SPS) system (DrSinter-SPS-5.40 MK-VI [21–23]) integrated with a glove box, as shown in Fig. SM1. Graphite dies with an internal diameter of 8.4 mm and a length of 30 mm were used, with graphite paper lining the die surfaces. One gram of UN powder was placed between graphite-paper layers and the upper and lower punches, as illustrated in Fig. 2a. The sintering parameters were selected primarily from literature data [24], which identify 75 MPa and 1923 K as suitable conditions and recommend an isothermal holding time of 5 min. These conditions were used to produce dense pellets, as summarized in Table 1. Sintering was performed under vacuum to minimize oxidation of the UN powder.

After sintering, the pellets were removed from the graphite die using a hydraulic press and prepared for polishing, as shown in Fig. 2b. The pellet surfaces were first ground using silicon-carbide papers with grit sizes ranging from 320 to 4000 to remove residual graphite foil and reduce surface

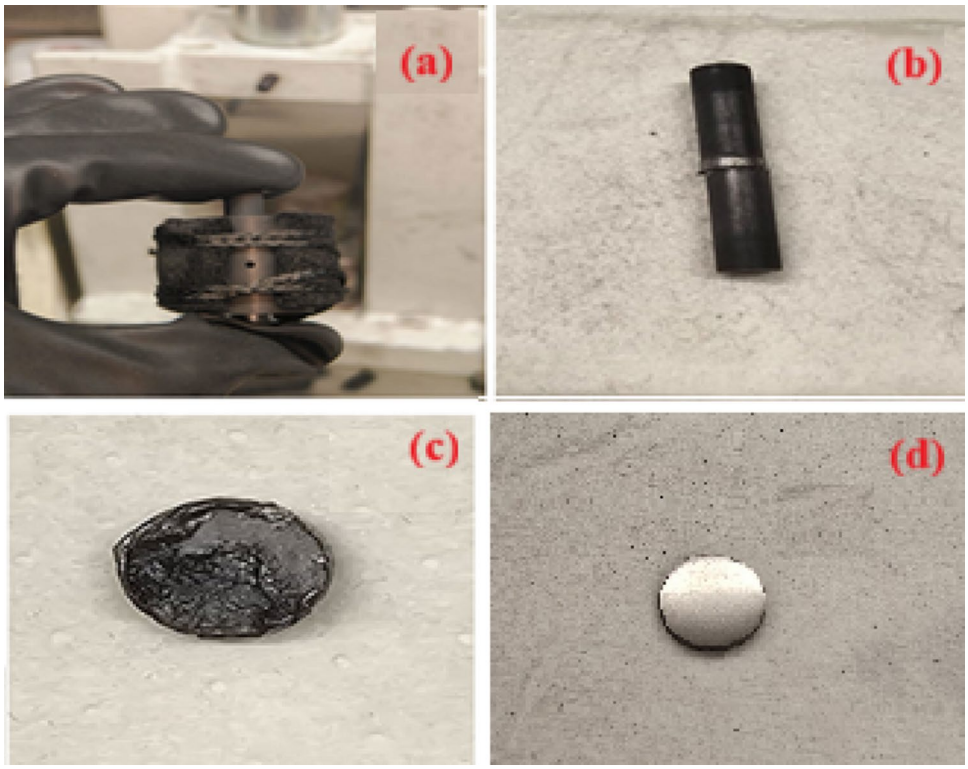



**Fig. 2** **a** Graphite die used for sintering. **b** The produced pellet between two punches. **c**,**d** Pellets before and after polishing, respectively

**Table 1** Die dimensions and sintering conditions

| Die inner diameter (mm) | Value | Sintering parameters | Value |
|---|---|---|---|
| Without graphite paper | 8.40 | Sintering pressure (MPa) | 75 |
| With graphite paper | 8.00 | Sintering temperature (K) | 1923 |
| | | Holding time (min) | 5 |

roughness. Final polishing was then performed to obtain a smooth, defect-free surface suitable for SEM analysis. This procedure consisted of polishing with a 1 µm diamond suspension on an MD-Nap cloth for several minutes, followed by polishing with a 1 µm colloidal silica suspension on an MD-Chem cloth for 10 min. Pellets before and after polishing are shown in Fig. 2c and d, respectively.

## Dissolution experiments

The dissolution behavior of uranium nitride (UN) pellets was investigated by analyzing both the solution phase and the pellet surface. Polished samples were examined by SEM to assess surface features that could influence dissolution. Dissolution experiments were performed in a 250 mL double-neck round-bottom flask equipped with a heating mantle, magnetic stirring, a condenser, and a thermometer adapter for temperature monitoring.

For each dissolution experiment, a 1 g UN pellet was contacted with 50 mL of nitric acid. Preliminary tests indicated that the dissolution behavior was not significantly affected by stirring rate; therefore, 500 rpm was used for all the experiments. The effect of agitation was also evaluated systematically at 250, 500, and 1000 rpm, as discussed in the "Results and discussion" section.

Based on previous studies of $UO_2$ dissolution in nitric acid, dissolution is commonly investigated over acid concentrations of approximately 4–10 M. Because uranium mononitride is expected to dissolve more readily than $UO_2$ under comparable conditions [25], nitric acid concentrations of 4, 6, and 8 M were selected. Experiments were performed at 323, 343, and 363 K to evaluate temperature effects and determine apparent activation energies.

Uranium concentrations were quantified by inductively coupled plasma mass spectrometry (ICP-MS; Thermo Fisher iCAP Q). For each sample, a 50 µL aliquot was withdrawn and diluted by a factor of $10^5$ to reduce the nitric acid concentration before measurement. Calibration standards spanning the expected analyte-concentration range were prepared for each measurement set, and blanks were included to correct for instrumental background (Fig. 3). Bismuth (Bi) was used as an internal standard for both calibration and sample measurements to improve reproducibility and accuracy. Before each measurement session, instrument performance was verified using the manufacturer's performance report, and blank and calibration-standard measurements were used to confirm appropriate instrument response and baseline correction.

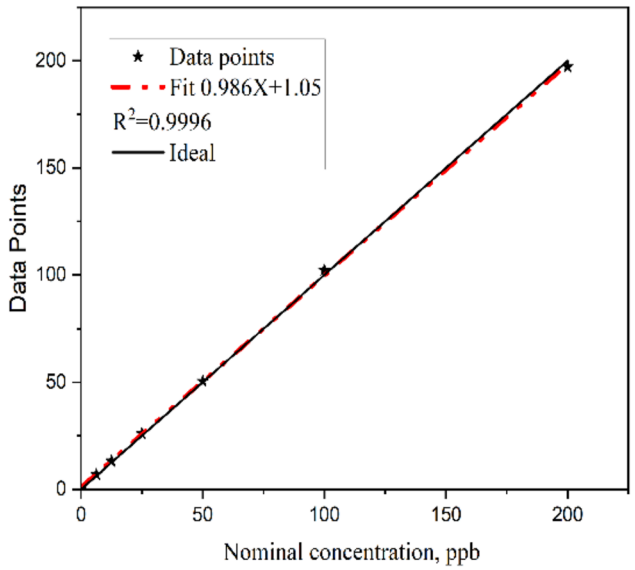



**Fig. 3** Calibration curve showing measured values as a function of nominal concentration over the range of 0–200 ppb

## Results and discussion

### XRD powder analysis

The XRD pattern of the synthesized UN powder is presented in Fig. 4. Using GSA-II, the lattice parameter of the synthesized UN powder was determined to be $0.4894 \pm 0.0001$ nm, which is slightly larger than the lattice parameter of pure UN (0.4889 nm), indicating the presence of some uranium carbide dissolved in the UN [26]. Based on a linear relationship between the lattice parameters of pure UN and UC, the synthesized UN powder was estimated to contain approximately $3500 \pm 700$ ppm carbon by weight, corresponding to a solid solution composition of $7 \pm 1.8\%$ UC dissolved in UN. The uncertainties reported for both the lattice parameter and the corresponding carbon content are presented as ±two standard deviations. This analysis does, however, ignore any effect that dissolved oxygen may have on the lattice parameter, since Vegard's law assumes the solid solution of only two compounds. It has been reported in [27] that oxygen exhibits low solubility in UN, but as the carbon level determination by XRD differs from the total carbon determination, it can still be that the lattice parameter is being affected by not only dissolved UC, but also some oxygen substitution for nitrogen in the UN solid solution lattice.

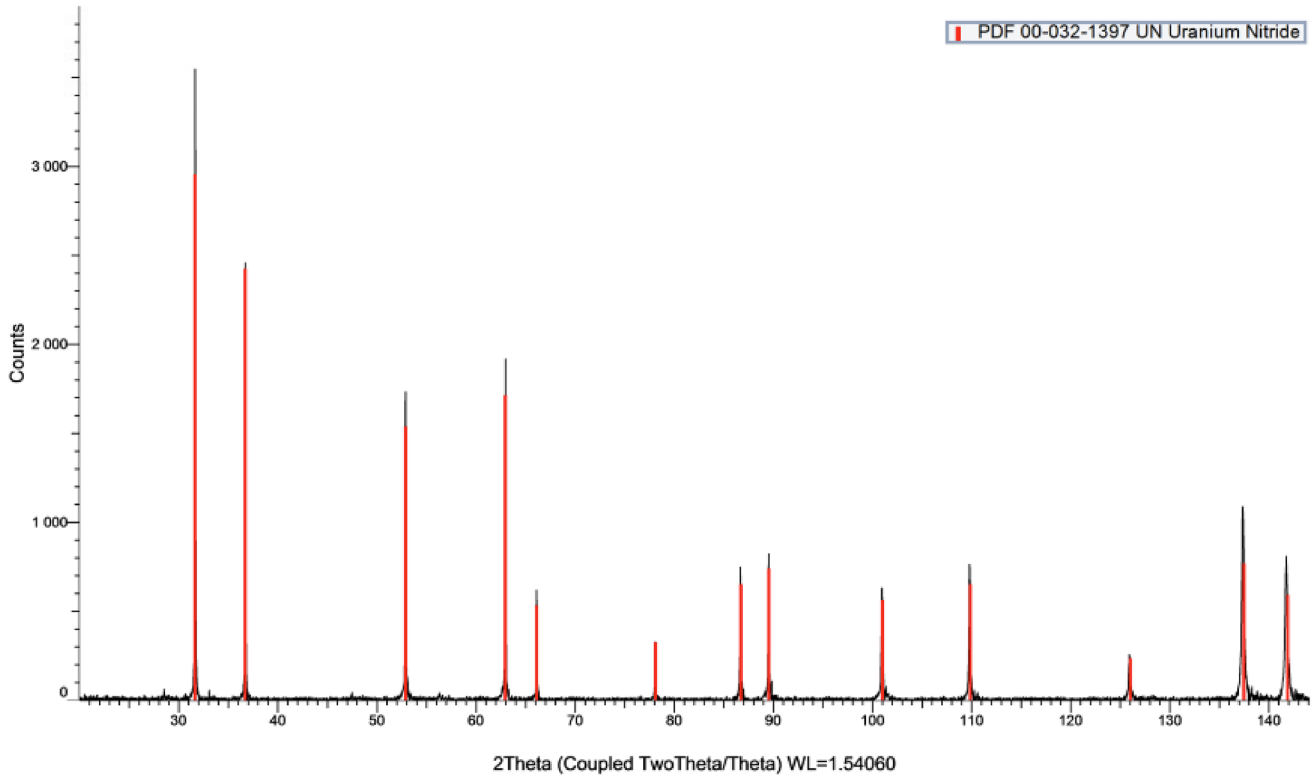



**Fig. 4** XRD of the synthesized uranium nitride powder

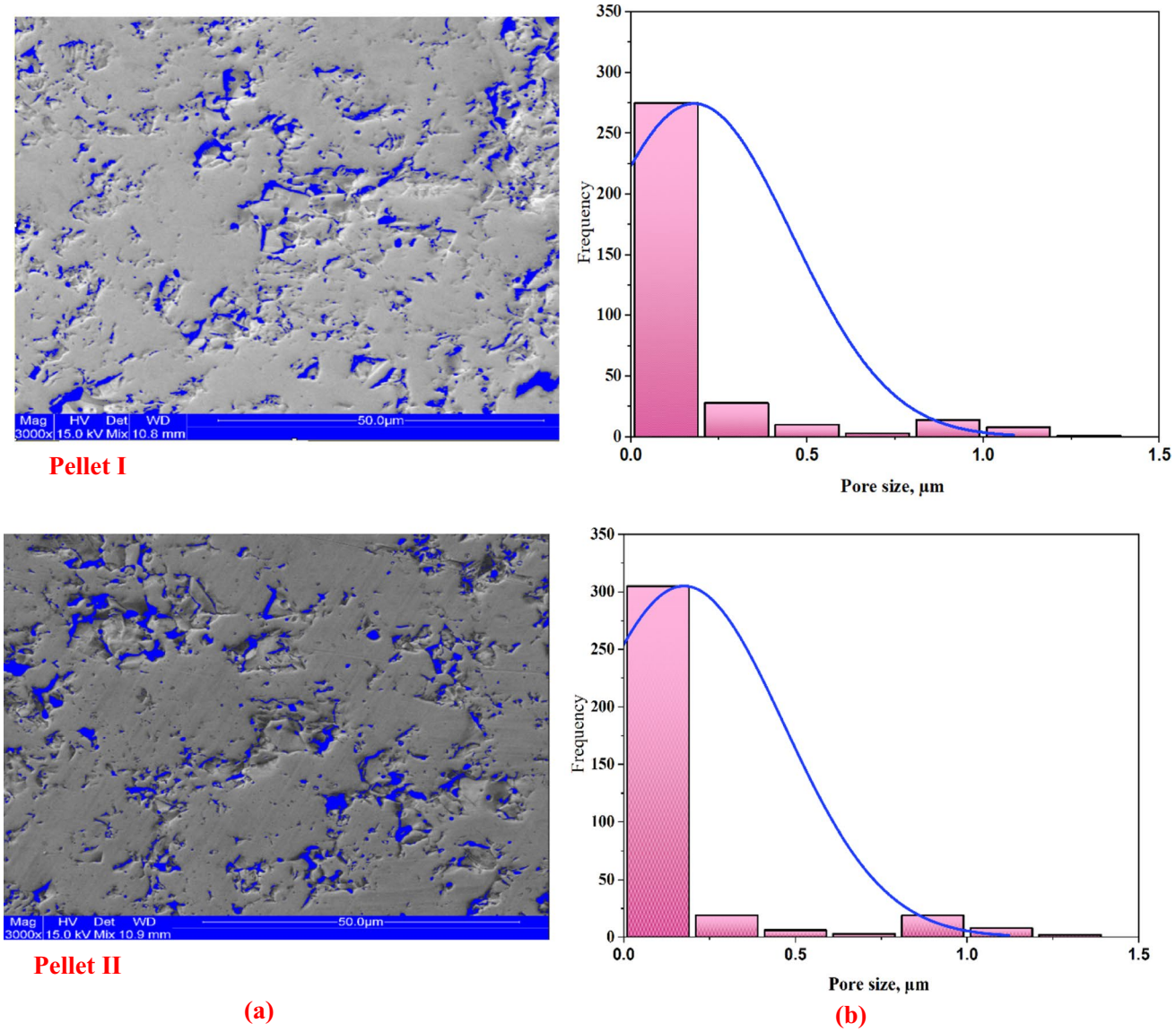



**Fig. 5** **a** SEM for two UN pellets, 15 kV and **b** pore-size distribution histogram

**Table 2** Physical characteristics of UN pellets used in the studies after polishing

| Property | Parameter | Value |
|---|---|---|
| Pellet dimensions | Weight (g) | 0.96–0.98 |
| | Height (mm) | 1.39–1.59 |
| | Diameter (mm) | 8.06–8.24 |
| Density | Theoretical density (g/cm$^3$) | 14.28 |
| | Geometrical density (%TD) | 90–92.5 |
| Porosity | Porosity (SEM) (%) | 10.0 ± 0.11 |
| | Porosity (Archimedes immersion) (%) | 7.3–7.5 ± 0.12 |

Total carbon analysis of the UN powder performed using a LECO CS-744 analyzer, measured 2570 ± 180 ppm carbon by weight and 45 ± 30 ppm sulfur. Both uncertainties are expressed as ±two standard deviations. Considering the measurement uncertainties, the two carbon levels are at the threshold of being significantly different from each other given the confidence interval used. Since the XRD analysis assumes only carbon and nitrogen are present in the UN, without accounting for sulfur or oxygen, and given the limitations of the tabletop XRD compared to modern full-size XRD instruments, the total carbon analysis is considered the more reliable measurement. Although the margin by which the two measurements differ is small, and overly strong conclusions should be avoided, the relative uncertainty of the XRD-based estimation is higher

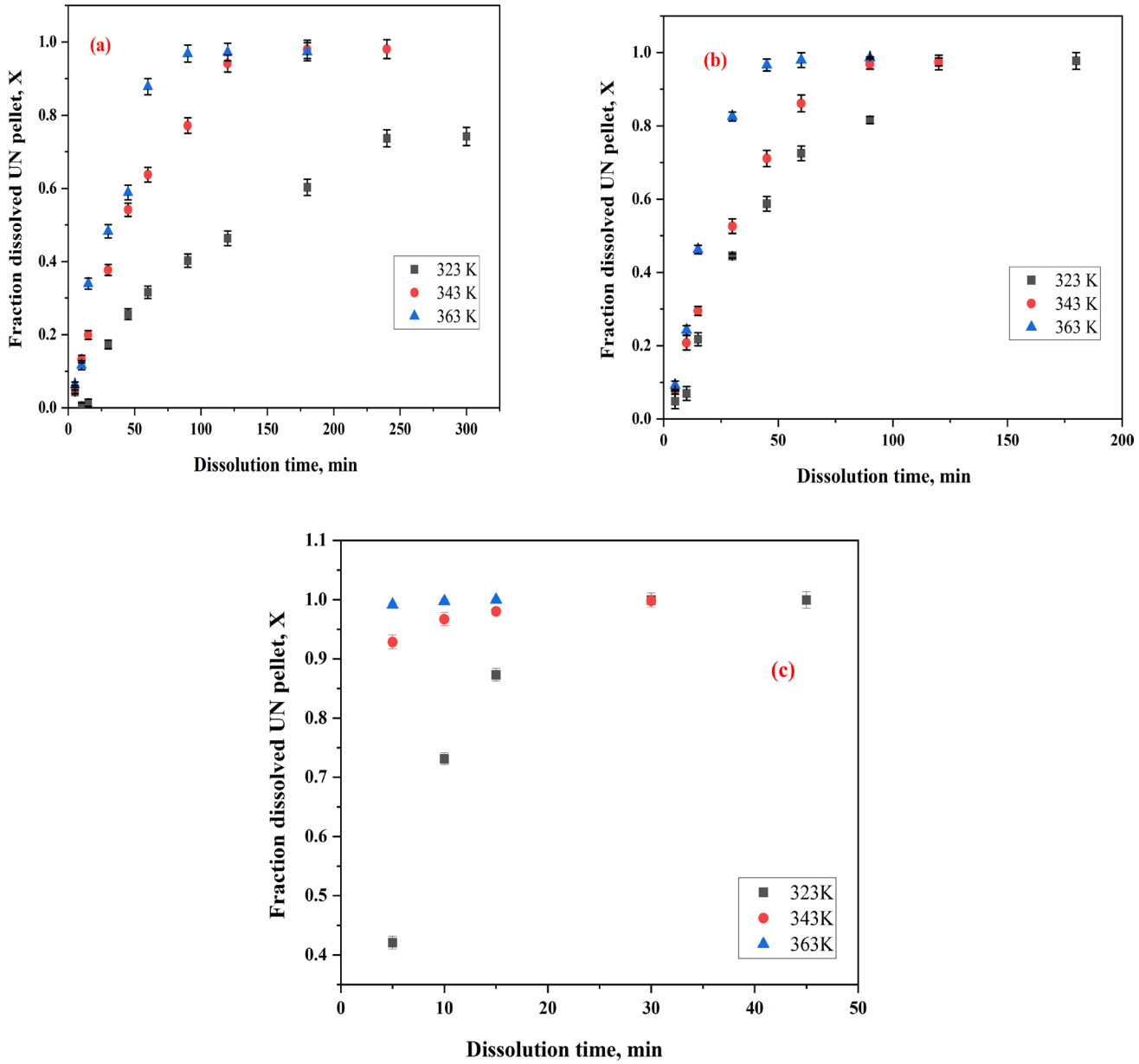



**Fig. 6** Fraction dissolved ($x$) versus dissolution time at different temperatures in **a** 4 M, **b** 6 M and **c** 8 M nitric acid

than that of the carbon analysis. Therefore, the carbon analysis is likely the more reliable indicator of the true carbon content in the synthesized UN powder.

After sintering, carbon measurements were taken on polished UN pellet shards. The results showed an increased carbon content of 5050 ± 910 ppm, suggesting a net carbon uptake during densification. This increase is attributed to carburization from graphite tooling or residual carbon in the sintering atmosphere, as during sintering, carbon may diffuse into the UN lattice or form uranium carbide phases, resulting in the observed increase in total carbon content of the final pellets.

The oxygen content in the sintered pellets was determined to be 1360 ± 490 ppm. This oxygen content is to be expected from UN fabricated by carbothermic nitridation, as the final oxygen in the material is difficult to completely remove. In Fig. 4, small diffraction peaks are observable at about 28.5°, 33°, 47.5° and 56.4° 2-theta. These peaks may appear to coincide with where the $UO_2$ (111), (200), (220) and (311) reflections should appear in the diffractogram, however, if looking closer, the peaks are shifted compared to where the $UO_2$ peaks should appear in the diffractogram. This is because the XRD used for the measurements does not completely filter out the k-beta radiation from

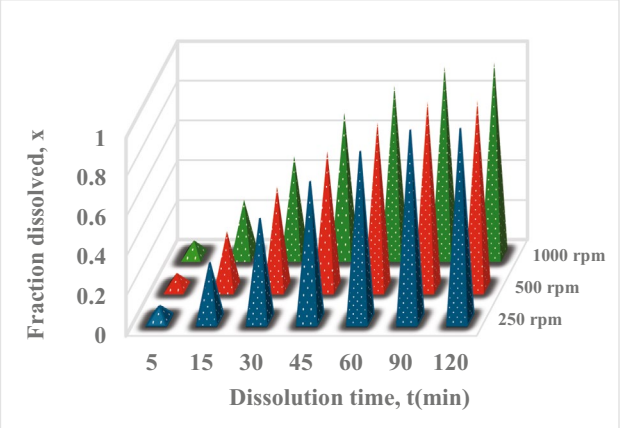



**Fig. 7** Dissolution process at different agitation rates, 6 M nitric acid and 343 K

the Cu-X-ray source. Thus, the peaks observed at about 28.6°, 33.1°, 47.5° and 56.4° 2-theta do not originate from $UO_2$, but are the UN reflections caused by Cu-k-beta radiation. The peaks at 28.6° and 33.1° 2-theta however can be caused both by $UO_2$ Cu-k-alpha diffraction and UN Cu-k-beta diffraction, therefore it is not reliable to conclude from the data how large phase fraction $UO_2$ remains in the sample, as the signal is distorted by UN Cu-k-beta signal of undetermined magnitude. For this reason, the total oxygen content measurement is more reliable predictor of the oxygen impurity level in the material. Given that the UN synthesis is conducted starting from $UO_2$, it is considered unlikely that no residual $UO_2$ would exist in the sample—if approximating all $1360 \pm 490$ ppm oxygen measured to be present as $UO_2$ in the sample, that would correspond to about $1.1 \pm 0.4\%$ $UO_2$ present in the UN.

## SEM and density measurements

The dimensions of the polished pellets were measured using a digital caliper (Fig. SM2). Based on pellet mass and dimensions, the geometrical density was 90–92.5% of the theoretical density of UN (14.28 g/cm$^3$). Porosity was also evaluated by the Archimedes immersion method using ethanol, which yielded values of $7.3–7.5 \pm 0.12\%$. Microstructural characterization was performed on representative pellets. Because all pellets were produced using identical SPS parameters, the analyzed specimens were considered representative of the full pellet set. SEM analysis (Fig. 5a), supported by ImageJ evaluation, confirmed a uniform uranium distribution. The pore-size distribution shown in Fig. 5b, together with the Gaussian fit, indicates that most pores were in the range of 0.1–0.5 µm. The porosity estimated from SEM was $10.0 \pm 0.11\%$, slightly higher than the value obtained by Archimedes immersion. This difference is consistent with the distinct measurement principles: SEM provides a local two-dimensional estimate from a polished section, whereas the Archimedes method provides a bulk estimate of liquid-accessible porosity. Nevertheless, both methods are consistent with the porosity range inferred from the geometrical density, approximately 7.5–10%, as summarized in Table 2.

## Effect of dissolution time and temperature

The dissolved fraction of uranium nitride as a function of time at different temperatures and nitric acid concentrations is shown in Fig. 6. The gradual increase in dissolved fraction demonstrates that dissolution proceeds over a measurable timescale rather than instantaneously. Dissolution was faster at higher temperatures and nitric acid concentrations, consistent with enhanced reaction kinetics [28]. However, these trends alone do not establish the rate-controlling mechanism; the kinetic-model analysis and agitation experiments discussed below provide a stronger basis for assessing reaction control. The time required for complete dissolution decreased substantially with increasing temperature and nitric acid concentration [29].

The dissolution behavior of the UN pellet exhibited a pronounced dependence on both $HNO_3$ concentration and temperature. At an $HNO_3$ concentration of 4 M, complete dissolution was achieved after approximately 120 min at 363 K and 180 min at 343 K, whereas at 323 K, complete dissolution was not attained within the investigated duration of 300 min. The residual pellet and the corresponding dissolution liquor obtained under these conditions are shown in Fig. SM3a and SM3b, respectively. Increasing the $HNO_3$ concentration to 6 M substantially enhanced the dissolution rate, reducing the time required for complete dissolution to approximately 60–120 min across the investigated temperature range. A further increase in acid concentration to 8 M resulted in markedly faster dissolution, with complete dissolution achieved within 30 min at 323 K, 15 min at 343 K, and 5 min at 363 K. These results demonstrate that the dissolution kinetics of UN are strongly accelerated by increasing both $HNO_3$ concentration and temperature. Qualitative observations indicated that $NO_x$ evolution increased with increasing nitric acid concentration and temperature. The formation of $NO_x$ was evidenced by the appearance of a brown-colored vapor phase above the reaction solution during most experiments. However, quantitative determination of $NO_x$ generation was not possible due to limitations of the available experimental equipment.

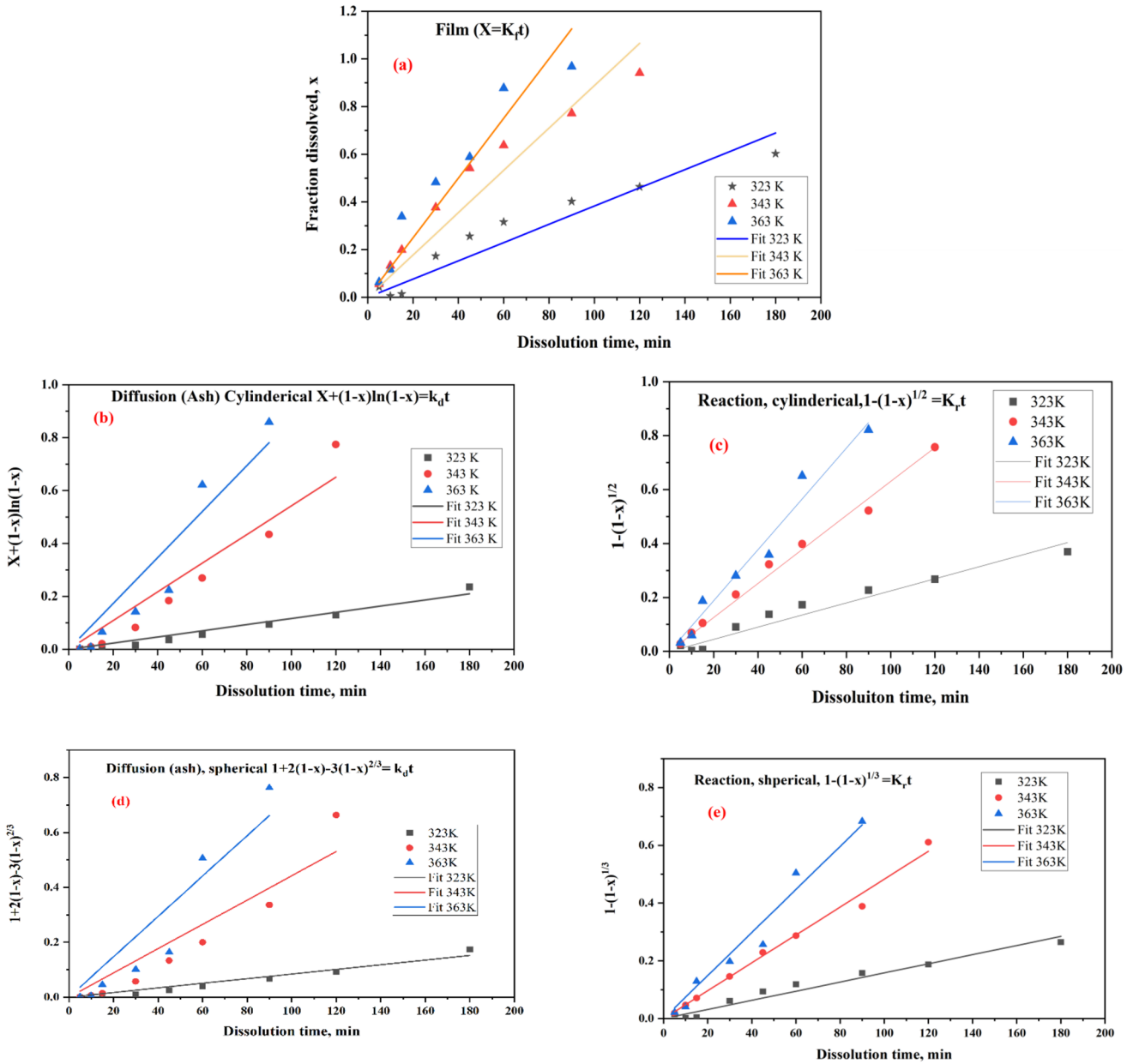



**Fig. 8** Linear fits of dissolution data in 4 M $HNO_3$ under different rate-controlling models: **a** film diffusion (spherical and cylindrical), **b** ash diffusion (cylindrical), **c** reaction control (spherical), **d** ash diffusion (spherical), and **e** reaction control (spherical)

## Effect of agitation

For the agitation experiments, 6 M $HNO_3$ was selected as the intermediate concentration within the investigated range of 4–8 M and was therefore considered representative for evaluating the effect of stirring. Agitation rates of 250, 500, and 1000 rpm were tested to assess whether external mass transfer influenced dissolution. As shown in Fig. 7, stirring rate had no significant effect on the dissolved fraction. On this basis, 500 rpm was selected for the subsequent experiments. The absence of a measurable stirring-rate effect is consistent with previously reported observations for uranium oxide and suggests that external film diffusion was not the dominant rate-limiting step under the investigated conditions.

## Kinetic modeling

The dissolution behavior of UN was evaluated using the shrinking-core model. Three rate-controlling mechanisms were considered: film diffusion, product-layer diffusion, and surface chemical reaction control. Both cylindrical and spherical particle geometries were evaluated. Kinetic plots

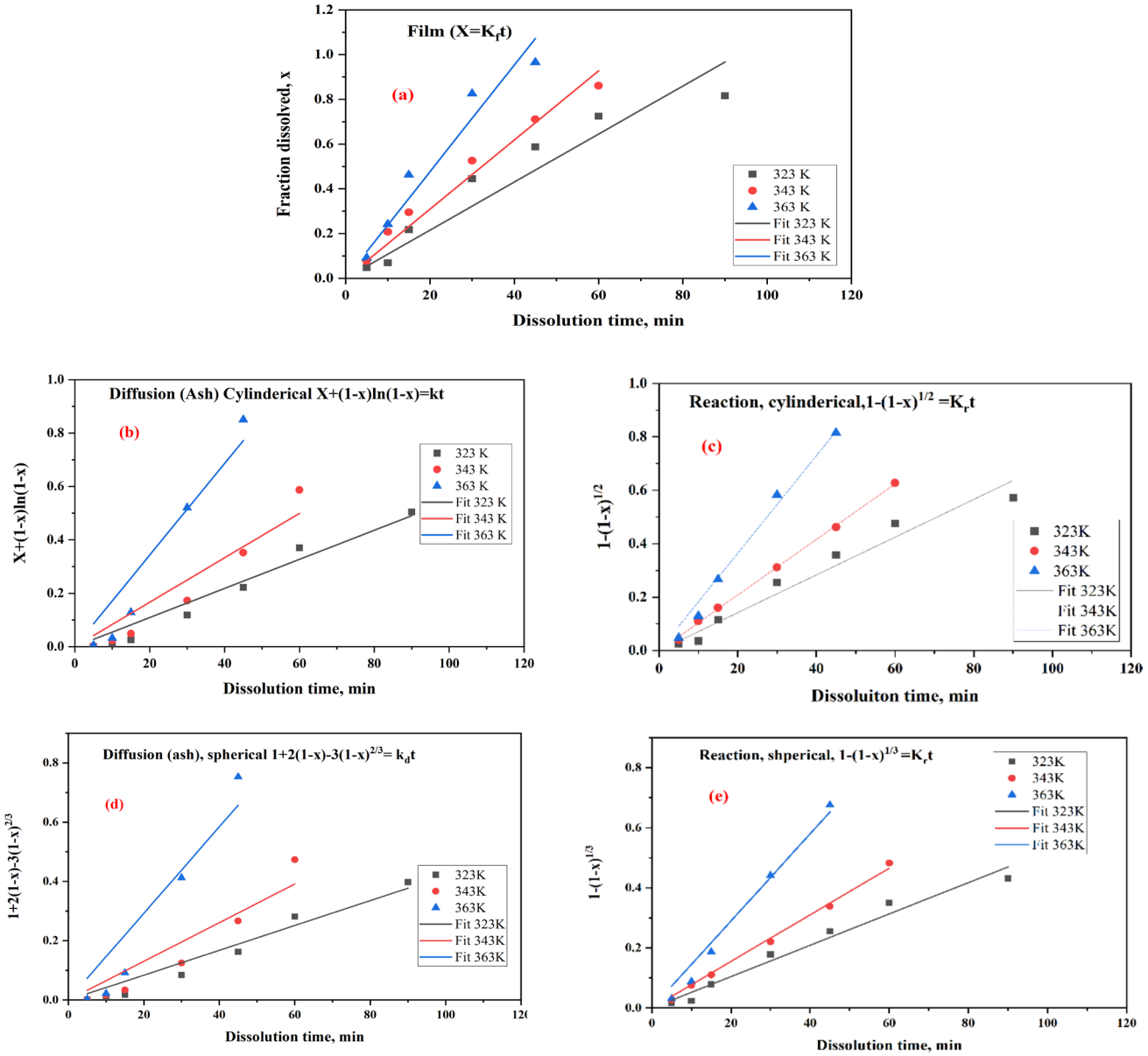



**Fig. 9** Linear fits of dissolution data in 6 M $HNO_3$ under different rate-controlling models: **a** film diffusion (spherical and cylindrical), **b** ash diffusion (cylindrical), **c** reaction control (spherical), **d** ash diffusion (spherical), and **e** reaction control (spherical)

for 323, 343, and 363 K in 4 and 6 M nitric acid are shown in Figs. 8 and 9.

Based on the regression analysis for the investigated temperatures and geometries (Tables 3, 4), the reaction-controlled shrinking-core models generally provided the highest coefficients of determination ($R^2 \approx 0.98$–$1.00$). Among the three temperatures, the data at 363 K exhibited the steepest slopes and therefore the highest apparent dissolution rates, followed by 343 and 323 K.

The residual-error distributions for dissolution in 4 and 6 M $HNO_3$, shown in Figs. 10 and 11, were generally centered around zero for all models. However, the reaction-controlled models exhibited the most uniform residual distributions and the least systematic deviation, indicating the best agreement with the experimental data.

Taken together, the residual-error distributions and $R^2$ values indicate that the surface-reaction models describe the experimental dissolution data better than the film-diffusion and product-layer-diffusion models under the investigated conditions. The diffusion-based models generally yielded lower $R^2$ values and greater deviations from linearity, suggesting that these mechanisms played a less dominant role in the overall dissolution behavior.

**Table 3** Reaction rate constants with $R^2$ values at various temperatures in 4 M nitric acid

| Model/geometry | Equation | Rate constant ($min^{-1}$) | 323 K | $R^2$ | 343 K | $R^2$ | 363 K | $R^2$ |
|---|---|---|---|---|---|---|---|---|
| Film diffusion (spherical or cylindrical) | $X=k_f t$ | $k_f$ | $0.0038 \pm 2.55317 \times 10^{-4}$ | 0.9613 | $0.0088 \pm 5.66231 \times 10^{-4}$ | 0.9683 | $0.01251 \pm 9.22207 \times 10^{-4}$ | 0.9631 |
| Cylindrical particle—ash diffusion | $X+(1-x)\ln(1-x)=k_d t$ | $k_d$ | $0.0011 \pm 6.64639 \times 10^{-5}$ | 0.9714 | $0.0054 \pm 4.27847 \times 10^{-4}$ | 0.9523 | $0.0086 \pm 8.85088 \times 10^{-4}$ | 0.9314 |
| Cylindrical particle—reaction control | $1-(1-x)^{1/2}=k_r t$ | $k_r$ | $0.0022 \pm 1.13359 \times 10^{-4}$ | 0.9774 | $0.0062 \pm 1.49143 \times 10^{-4}$ | 0.9955 | $0.0094 \pm 4.18606 \times 10^{-4}$ | 0.9863 |
| Spherical particle—ash diffusion | $1+2(1-x)-3(1-x)^{2/3}=k_d t$ | $k_d$ | $0.0008 \pm 5.29468 \times 10^{-5}$ | 0.9655 | $0.0044 \pm 4.43081 \times 10^{-4}$ | 0.9249 | $0.00735 \pm 6.81856 \times 10^{-4}$ | 0.9111 |
| Spherical particle—reaction control | $1-(1-x)^{1/3}=k_r t$ | $k_r$ | $0.00158 \pm 7.14475 \times 10^{-5}$ | 0.9819 | $0.00482 \pm 1.25922 \times 10^{-4}$ | 0.9945 | $0.00745 \pm 3.65927 \times 10^{-4}$ | 0.9833 |

**Table 4** Reaction rate constants with $R^2$ values at various temperatures in 6 M nitric acid

| Model/geometry | Equation | Rate constant ($min^{-1}$) | 323 K | $R^2$ | 343 K | $R^2$ | 363 K | $R^2$ |
|---|---|---|---|---|---|---|---|---|
| Film diffusion (spherical or cylindrical) | $X=k_f t$ | $k_f$ | $0.0107 \pm 8.15842 \times 10^{-4}$ | 0.961016 | $0.0154 \pm 6.683 \times 10^{-4}$ | 0.988903 | $0.0238 \pm 1.64163 \times 10^{-3}$ | 0.9767 |
| Cylindrical particle—ash diffusion | $X+(1-x)\ln(1-x)=k_d t$ | $k_d$ | $0.0054 \pm 3.52411 \times 10^{-4}$ | 0.971436 | $0.0083 \pm 8.54404 \times 10^{-4}$ | 0.939926 | $0.0171 \pm 1.93166 \times 10^{-3}$ | 0.9396 |
| Cylindrical particle—reaction control | $1-(1-x)1/2=k_r t$ | $k_r$ | $0.00707244 \pm 3.61789 \times 10^{-4}$ | 0.981965 | $0.0104005 \pm 8.52338 \times 10^{-5}$ | 0.999597 | $0.0182254 \pm 6.79863 \times 10^{-4}$ | 0.9930 |
| Spherical particle—ash diffusion | $1+2(1-x)-3(1-x)2/3=k_d t$ | $k_d$ | $0.00419359 \pm 2.94817 \times 10^{-4}$ | 0.9664 | $0.00651625 \pm 7.63483 \times 10^{-4}$ | 0.922923 | $0.0146096 \pm 1.88003 \times 10^{-3}$ | 0.9223 |
| Spherical particle—reaction control | $1-(1-x)1/3=k_r t$ | $k_r$ | $0.00521917 \pm 2.26691 \times 10^{-4}$ | 0.986942 | $0.00775579 \pm 1.46373 \times 10^{-4}$ | 0.997867 | $0.0144991 \pm 6.98834 \times 10^{-4}$ | 0.9884 |

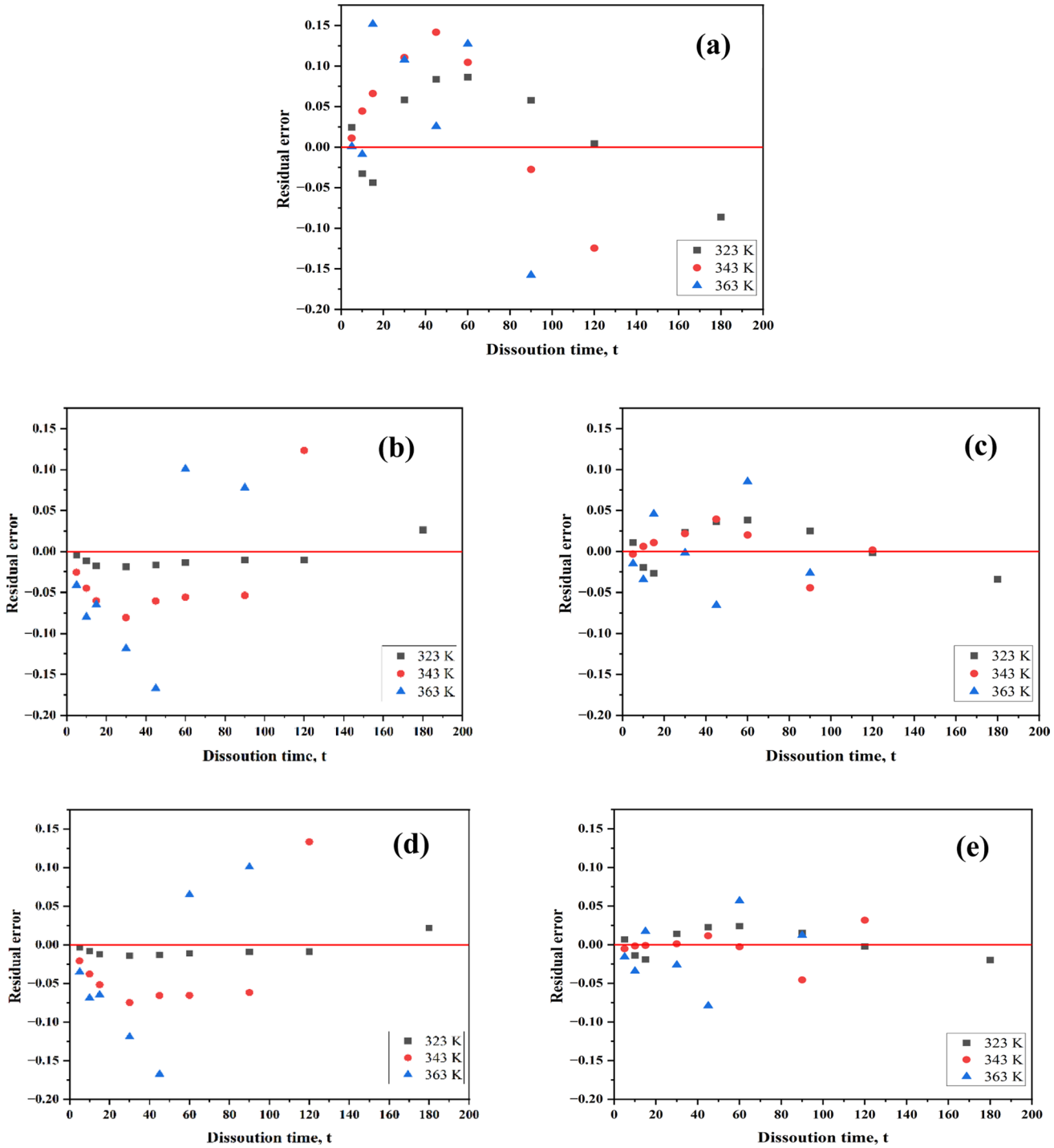



**Fig. 10** Residual error for dissolution data in 4 M $HNO_3$ under different rate-controlling models: **a** film diffusion (spherical and cylindrical), **b** ash diffusion (cylindrical), **c** reaction control (spherical), **d** ash diffusion (spherical), and **e** reaction control (spherical)

Overall, more than one transport or reaction process may contribute to UN dissolution. Nevertheless, the comparatively better agreement with the reaction-controlled shrinking-core models indicates that surface chemical reaction was the predominant rate-controlling contribution under the investigated conditions [30].

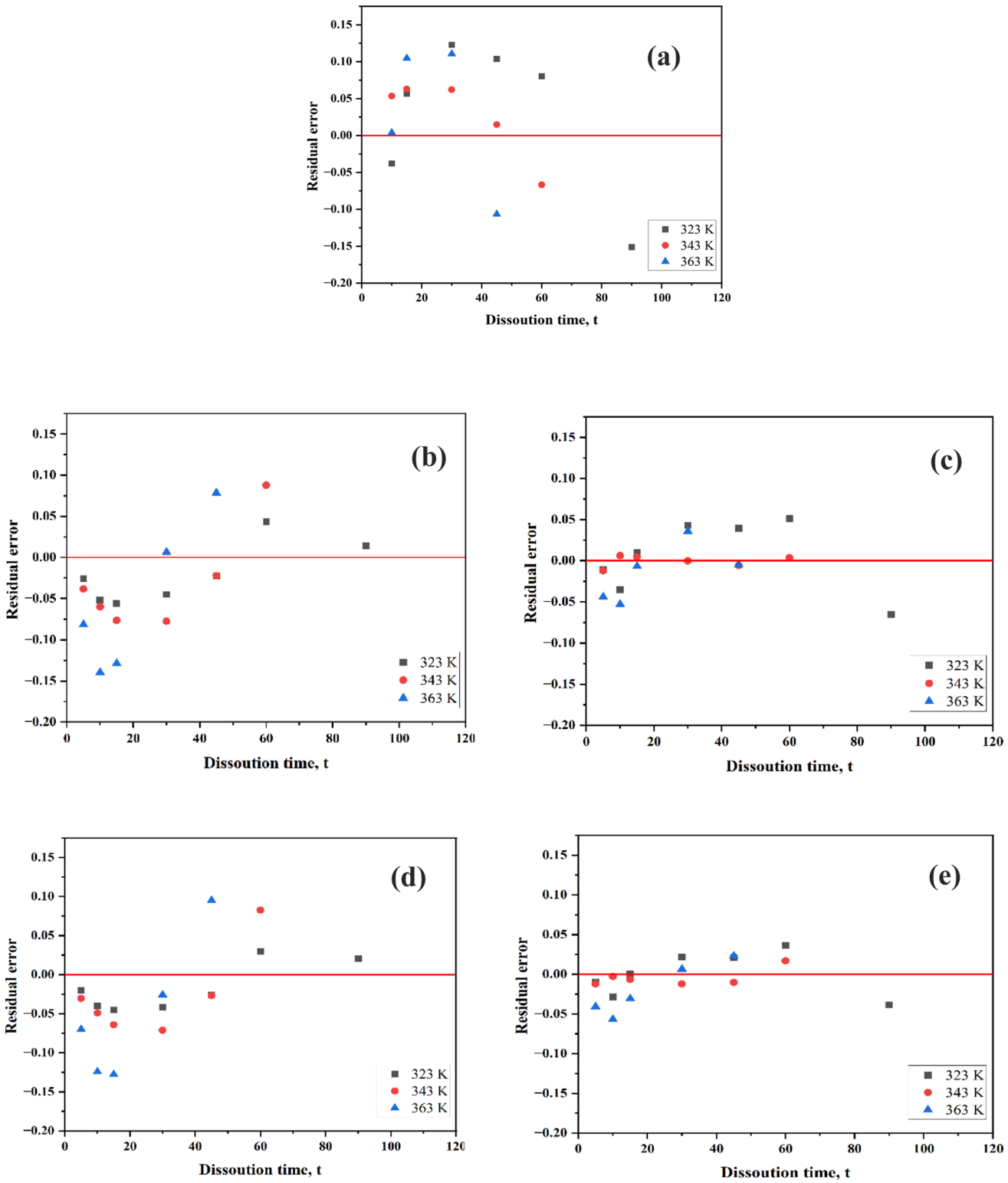



**Fig. 11** Residual error for dissolution data in 6 M $HNO_3$ under different rate-controlling models: **a** film diffusion (spherical and cylindrical), **b** ash diffusion (cylindrical), **c** reaction control (spherical), **d** ash diffusion (spherical), **e** reaction control (spherical)

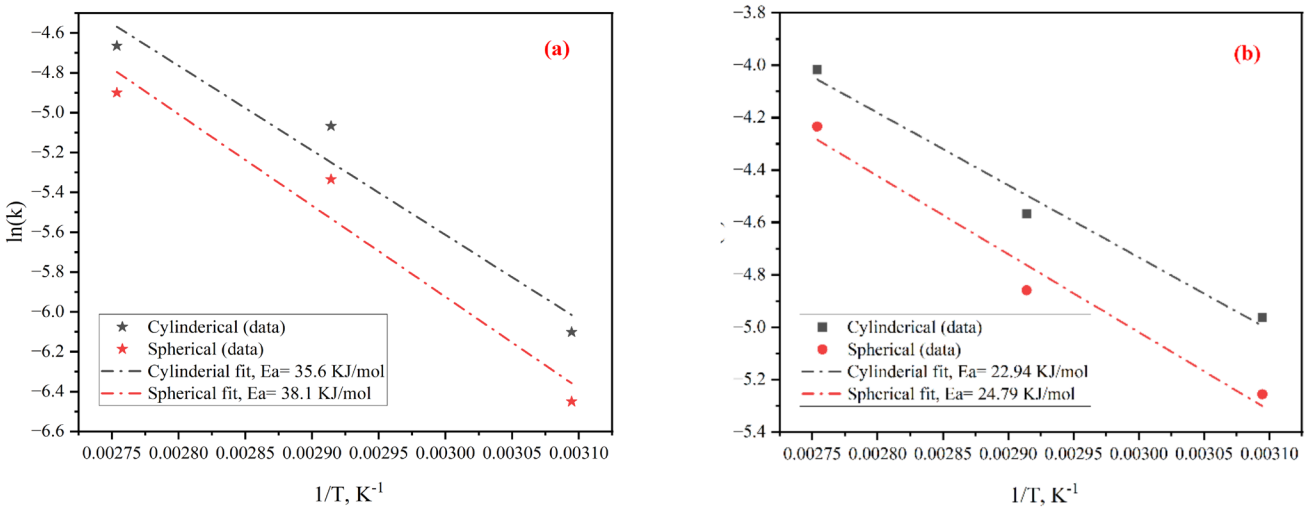



**Fig. 12** Ln($K$) vs. 1/$T$ with **a** 4 M and **b** 6 M nitric acid

**Table 5** Activation energy values (kJ/mol) at varying concentrations of nitric acid

| Kinetic parameters | Nitric acid concentration | | | |
|---|---|---|---|---|
| | 4 M | | 6 M | |
| | Cylindrical particle | Spherical particle | Cylindrical particle | Spherical particle |
| $E_a$ (kJ/mol) | 35.29 | 38.1 | 22.94 | 24.79 |
| $R^2$ | 0.908 | 0.909 | 0.968 | 0.947 |

## Activation energy calculation

The temperature dependence of the apparent reaction-rate constant was evaluated using the Arrhenius equation. Figure 12 presents plots of ln($K$) versus reciprocal temperature (1/$T$), constructed from experimentally determined rate constants at three temperatures. The approximately linear relationships are consistent with Arrhenius-type behavior over the investigated temperature range, while the negative slopes reflect the expected increase in reaction rate with increasing temperature.

As summarized in Table 5, the apparent activation energies ranged from 35.29 to 38.10 kJ/mol in 4 M $HNO_3$ and from 22.94 to 24.79 kJ/mol in 6 M $HNO_3$. These values, together with the kinetic-model results, suggest a substantial contribution from surface chemical reactions rather than purely diffusional control. The lower apparent activation energies obtained at 6 M $HNO_3$ further indicate that increasing the nitric acid concentration alters the apparent kinetic barrier associated with UN dissolution. Moreover, the similar activation-energy values obtained using cylindrical and spherical geometries suggest that the assumed particle geometry has only a minor influence on the inferred kinetic behavior.

Previous studies have proposed an autocatalytic mechanism for $UO_2$ dissolution in nitric acid, in which nitrous acid ($HNO_2$) acts as an important oxidizing species. Although this mechanism has been established specifically for $UO_2$, related reaction pathways may also contribute under the present experimental conditions. An increase in nitric acid concentration may promote the formation or activity of $HNO_2$, thereby contributing to the enhanced dissolution rate observed at higher $HNO_3$ concentrations [15, 17, 18, 30, 31].

## Conclusion

Uranium nitride (UN) was successfully synthesized from $UO_2$ powder by carbothermic nitridation and consolidated into pellets by spark plasma sintering. The gravimetric synthesis yield was not determined; however, complete stoichiometric conversion of $UO_2$ to UN would correspond to a theoretical UN mass of approximately 93.3% of the initial $UO_2$ mass. XRD confirmed the formation of UN, while carbon and oxygen content measurements revealed the presence of carbon and oxygen impurities. The sintered pellets reached 90–92.5% of the theoretical density and exhibited porosity consistent with the geometrical-density, Archimedes, and SEM measurements. Dissolution experiments in 4, 6, and 8 M $HNO_3$ at 323, 343, and 363 K showed that the dissolution rate increased markedly with both acid concentration and temperature. Complete dissolution was achieved under several conditions, with the shortest dissolution times observed in 8 M $HNO_3$. Analysis using the shrinking-core model showed that surface-reaction control provided a better description of the experimental data than film-diffusion or product-layer-diffusion control. Apparent activation energies of 35.29–38.10 kJ/

mol in 4 M $HNO_3$ and 22.94–24.79 kJ/mol in 6 M $HNO_3$ were consistent with a predominantly reaction-controlled dissolution process under the investigated conditions. Future work should incorporate real-time $NO_x$ measurements to clarify the role of nitrogen-containing reaction products and to evaluate the possible autocatalytic contribution of $HNO_2$ to UN dissolution.

**Supplementary Information** The online version contains supplementary material available at https://doi.org/10.1007/s10967-026-11182-7.

**Author contributions** M. Ghaly: Investigation, Methodology, Data curation, Formal analysis, Software, Visualization, Conceptualization, Validation, Writing-original draft. Teodora Retegan Vollmer: Conceptualization, Validation, Visualization, Project administration, Supervision, Funding acquisition. G. Zagoraios: SPS methodology, review & editing. Esraa Darwish: ICP-MS analysis Christos Andrikopoulos: SPS methodology, Marcus Hedberg: Supervision, Methodology, Analysis support, Conceptualization, Validation, Writing—review & editing.

**Funding** Open access funding provided by Chalmers University of Technology. This publication was funded by the European Union within the FREDMANS project, ECGA No. 101060800. We wish to thank Chelsea Foreman for proofreading the manuscript.

**Data availability** No datasets were generated or analysed during the current study.

## Declarations

**Conflict of interest** The authors declare no competing interests.

**Open Access** This article is licensed under a Creative Commons Attribution 4.0 International License, which permits use, sharing, adaptation, distribution and reproduction in any medium or format, as long as you give appropriate credit to the original author(s) and the source, provide a link to the Creative Commons licence, and indicate if changes were made. The images or other third party material in this article are included in the article's Creative Commons licence, unless indicated otherwise in a credit line to the material. If material is not included in the article's Creative Commons licence and your intended use is not permitted by statutory regulation or exceeds the permitted use, you will need to obtain permission directly from the copyright holder. To view a copy of this licence, visit http://creativecommons.org/licenses/by/4.0/.

## References

1. Jones S, Boxall C, Maher C, Taylor R (2023) A review of the reprocessability of uranium nitride based fuels. Prog Nucl Energy 165:104917. https://doi.org/10.1016/j.pnucene.2023.104917
2. Aneheim E, Hedberg M (2016) Dissolution performance of plutonium nitride based fuel materials. Proc Chem 21:231–238. https://doi.org/10.1016/j.proche.2016.10.033
3. Minato K, Akabori M, Takano M, Arai Y, Nakajima K, Itoh A, Ogawa T (2003) Fabrication of nitride fuels for transmutation of minor actinides. J Nucl Mater 320:18–24
4. IAEA (2003) Status and advances in MOX fuel technology. Technical reports series, 179 pp
5. Dalger T, Szenknect S, Tocino F, Claparede L, Mesbah A, Moisy P, Dacheux N (2018) Kinetics of dissolution of $Th_{0.25}U_{0.75}O_2$ sintered pellets in various acidic conditions. J Nucl Mater 510:109–122. https://doi.org/10.1016/j.jnucmat.2018.07.050
6. Khot PM, Singh G, Shelke BK, Surendra B, Yadav MK, Mishra AK, Afzal M, Panakkal JP (2014) Development of recycling processes for clean rejected MOX fuel pellets. Nucl Eng Des 270:227–237. https://doi.org/10.1016/j.nucengdes.2013.12.060
7. Singh G, Khot PM, Kumar P, Bhatt RB, Behere PG, Afzal M (2017) Microwave based oxidation process for recycling the off-specification (U, Pu)$O_2$ fuel pellets. J Nucl Mater 484:81–90. https://doi.org/10.1016/j.jnucmat.2016.11.024
8. Mernache F, Boutarek N, Bouchemaa T, Kaim A, Hadji S (2016) Recycling process of defective aged uranium dioxide pellets. J Nucl Sci Technol 53:790–796. https://doi.org/10.1080/00223131.2015.1072483
9. Desigan N, Bhatt NP, Pandey NK, Kamachi Mudali U, Natarajan R, Joshi JB (2017) Mechanism of dissolution of nuclear fuel in nitric acid relevant to nuclear fuel reprocessing. J Radioanal Nucl Chem 312:141–149. https://doi.org/10.1007/s10967-017-5208-z
10. Desigan N, Augustine E, Murali R, Pandey NK, Kamachi Mudali U, Natarajan R, Joshi JB (2015) Dissolution kinetics of Indian PHWR natural $UO_2$ fuel pellets in nitric acid—effect of initial acidity and temperature. Prog Nucl Energy 83:52–58. https://doi.org/10.1016/j.pnucene.2015.03.001
11. Marc P, Magnaldo A, Vaudano A, Delahaye T, Schaer É (2017) Dissolution of uranium dioxide in nitric acid media: what do we know? EPJ N-Nucl Sci Technol 3:13. https://doi.org/10.1051/epjn/2017005
12. Clarens F, De Pablo J, Casas I, Giménez J, Rovira M, Merino J, Cera E, Bruno J, Quiñones J, Martínez-Esparza A (2005) The oxidative dissolution of unirradiated $UO_2$ by hydrogen peroxide as a function of pH. J Nucl Mater 345:225–231. https://doi.org/10.1016/j.jnucmat.2005.06.002
13. Momotov VN, Erin EA, Volkov AY, Khamdeev MI, Tikhonova DE, Lakeev PV, Dvoeglazov KN (2023) Dissolution of mixed nitride uranium-plutonium spent nuclear fuel. Radiochemistry 65:311–322. https://doi.org/10.1134/S1066362223030062
14. Arm ST, Wierschke JB (2024) Concepts for actinide recovery from TRISO used nuclear fuel. www.osti.gov
15. Uriarte AL, Rainey RH (1965) Dissolution of high-density $UO_2$, $PuO_2$, and $UO_2$–$PuO_2$ pellets in inorganic acids. Oak Ridge National Laboratory
16. Herrmann B (1984) Dissolution of unirradiated $UO_2$-pellets in nitric acid. Kernforschungszentrum Karlsruhe GmbH, Germany
17. Taylor RF, Sharratt EW, Chazal LEM, Logsdail DH (1963) Dissolution rates of uranium dioxide sintered pellets in nitric acid systems. J Appl Chem 13:32–40
18. Yasuike Y, Ikeda Y, Takashima Y, Chikazawa T, Nishimura K, Hasegawa S (1995) Kinetic study on dissolution of $U_3O_8$ powders in nitric acid. J Nucl Sci Technol 32:596–598. https://doi.org/10.3327/jnst.32.596
19. Thomas GF, Till G (1984) The dissolution of unirradiated $UO_2$ fuel pellets under simulated disposal conditions. Nucl Chem Waste Manag 5:141–147. https://doi.org/10.1016/0191-815X(84)90044-5
20. Levenspiel O (1999) Ch. 25: Fluid-Particles Reaction: Kinetics. In: Chemical Reaction Engineering. John Wiley & Sons, New York, NY, pp 566-577
21. Ge L, Subhash G, Baney RH, Tulenko JS, McKenna E (2013) Densification of uranium dioxide fuel pellets prepared by spark plasma sintering (SPS). J Nucl Mater 435:1–9. https://doi.org/10.1016/j.jnucmat.2012.12.010
22. Chen Z, Subhash G, Tulenko JS (2014) Master sintering curves for $UO_2$ and $UO_2$–SiC composite processed by spark plasma sintering. J Nucl Mater 454:427–433. https://doi.org/10.1016/j.jnucmat.2014.08.023
23. Greenquist I, Tonks MR, Zhang Y (2018) Review of sintering and densification in nuclear fuels: physical mechanisms, experimental

results, and computational models. J Nucl Mater 507:381–395. https://doi.org/10.1016/j.jnucmat.2018.03.046
24. Johnson KD, Wallenius J, Jolkkonen M, Claisse A (2016) Spark plasma sintering and porosity studies of uranium nitride. J Nucl Mater 473:13–17. https://doi.org/10.1016/j.jnucmat.2016.01.037
25. Fan W, Zhao W, You L, Song X, Zhang W, Yu H, Sun S (2004) A simple method to synthesize single-crystalline lanthanide orthovanadate nanorods. J Solid State Chem 177:4399–4403
26. Holleck H, Smailos E, Thuemmler F (1969) Zur mischphasenbildung der mononitride in den systemen u- (y, la, pr)-n. J Nucl Mater 32:281–289
27. Jain GC, Ganguly C (1993) Experimental evaluation of oxygen solubility in UN, PuN and (U, Pu) N. J Nucl Mater 202:245–251
28. Bensmain B, Chegrouche S, Barkat M, Mellah A, Nibou D (2016) The dissolution of uranium oxides: thermodynamic and kinetic investigations. Hydrometallurgy 160:73–78. https://doi.org/10.1016/j.hydromet.2015.12.003
29. Ferris LM (1968) Reactions of uranium mononitride, thorium monocarbide and uranium monocarbide with nitric acid and other aqueous reagents. J Inorg Nucl Chem 30(10):2661–2669. https://doi.org/10.1016/0022-1902(68)80393-8
30. Smain K, Hanane B, Nacera A (2020) Recycling scrap from Unirradiated nuclear fuel by $HNO_3$ leaching. Chem Afr 3:343–350. https://doi.org/10.1007/s42250-020-00134-7
31. Zhao Y, Chen J (2008) Studies on the dissolution kinetics of ceramic uranium dioxide particles in nitric acid by microwave heating. J Nucl Mater 373:53–58. https://doi.org/10.1016/j.jnucmat.2007.03.271

**Publisher's Note** Springer Nature remains neutral with regard to jurisdictional claims in published maps and institutional affiliations.